NUMERICAL AND EXPERIMENTAL INVESTIGATIONS FOR SUPER SONIC ACTIVE FLOW CONTROL IN THE TRANSONIC MACH REGIME

Carola Ebert*, Jan Mihalyovics†,
Marcel Staats*, Dieter Peitsch†, Julien Weiss*
Technical University of Berlin, Institute of Aeronautics and Astronautics,
Marchstr. 12, 10587 Berlin, Deutschland

Abstract

In the present paper, an experimental investigation on the application of high-speed sweeping jet actuators was carried out. It examines the feasibility of a super sonic exit jet to control boundary layer separation caused by an adverse pressure gradient in a compressible Mach number regime. The first part of the investigation includes a thorough assessment of the used sweeping jet actuator by three dimensional numerical simulations using OpenFoam®. A validation of the results was done by means of schlieren visualization within the actuator and dynamic pressure measurements at the actuator outlet. The outlet signal of the actuator features a characteristic switching frequency of $f_s \approx 1200$ Hz and a peak Mach number of $Ma \approx 1.4$ which was evident in the experiments and the CFD simulation. The supply pressure ratio of the actuator was set to $PR = 3.6$ using compressed air. The second part of the paper presents the results of the wind tunnel experiments using a test section with the geometry of a half-diffusor ramp equipped with two sweeping jet actuators. Inflow conditions of Mach numbers ranging from $Ma_\infty = 0.3$ to $Ma_\infty = 0.8$ were investigated. The conducted wind tunnel experiments include detailed oil flow surface visualizations and mean surface pressure measurements in order to demonstrate the impact of the active flow control system. By varying the mass flow rate of the actuator system different operating points were studied. The presented results indicate the positive effect of active flow control regarding the pressure rise over the ramp in a compressible Mach number regime. The separated flow region was significantly reduced.

Keywords

active flow control; fluidic actuators; transsonic flow; numerical simulation, experimental measurements, sweeping jet actuator

1 INTRODUCTION

The reduction of aircraft engine emissions as well as the efficient conversion of energy using gas turbines calls for disruptive technologies to go beyond the most efficient projected improvements in current technologies. Amongst others, achieving this goal requires a ground breaking improvement of flow control devices to push engine efficiencies beyond their current limits and improve their operability. Despite the vast range of existing flow control solutions, most of the active flow control (AFC) systems described in the literature are still far from being implemented on turbo engine relevant flow phenomena.

In earlier investigations by Troutt et al. [1] it was shown that the most effective Strouhal-number range for the actuation of boundary layers can be assumed to be approximately constant over a wide range of Reynolds numbers. Thus, the forcing mechanism is independent of Reynolds number driven effects. Nevertheless, Nagib et al. [2] showed that efficient forcing is only possible with a correspondingly high velocity ratio (VR). The VR has a significant impact on the control authority of AFC measures e.g. in axial turbo compressors.

Taking the flow in a high-pressure compressor stage into account, the inflow conditions are compressible and a strong adverse pressure gradient exist. Due to that, the flow field in axial compressors is dominated by highly complex flow patterns and flow separations that cause losses and limit the operating range of the component [3].

A promising way to increase the efficiency and stability of a high turning compressor stator is actively controlling these secondary flow features. In order to use AFC measures to influence the flow around high turning stator blades in a transonic Mach number regime, actuators featuring a super

*Chair of Aerodynamics
†Chair for Aero Engines

doi:10.25967/490165

sonic exit jet have to be used to reach a sufficient velocity ratio. These measures lead to higher pressure recoveries of a stator vane and a reduction of flow losses [4].
Scientific research in recent decades largely focused on the investigation of fundamental influencing methods using AFC. According to the current state of the art, however, self-switching fluidic actuators – such as the sweeping jet (SWJ) actuator – are known which are already successfully used with high TRL and even in flight tests to influence the external flows on aircraft ([5], [6] and [7]). Nevertheless, an integration of such high-speed fluidic actuators into a turbo machine relevant compressible flow of axial compressors could not yet be demonstrated until now.
Trávníček et al. [8] attempted to reduce the flow separation in a compressible compressor cascade using continuous and periodic blowing at the suction side. However, results showed a minor effect of the actuators due to a sub sonic exit jet.
The objective of the present work is to investigate the feasibility of active flow control in a compressible Mach number regime. Therefore, the test section of a transonic wind tunnel was equipped with a half-diffusor ramp model, generating a pressure-induced flow separation. The inflow condition of the wind tunnel experiments were ranging from $Ma = 0.3$ to $Ma = 0.8$, corresponding to Reynolds numbers of $Re = 0.4 - 1.1 \cdot 10^6$ with respect to the ramp height. The flow pattern over the ramp is dominated by complex secondary flow structures. For the application of active flow control, two SWJ actuators were implemented at the separation line. The operating point of the actuator system was varied by adjusting the actuator supply mass flow rate. It was successfully demonstrated that the separated flow reattaches in the mid section of the ramp by means of active flow control, producing a super sonic exit jet. Oil flow visualization and static pressure measurements along the ramp were conducted to evaluate the efficiency of the actuation system.

2 ACTUATOR CHARACTERISTICS

In a first step, a numerical simulation of the inner flow field of a single SWJ actuator was performed. The experimental validations of the CFD simulation were carried out using dynamic pressure measurements along the actuator outlet slot and schlieren visualization of the actuator inner flow field - extracted from [9]. Furthermore, the performance of the actuator power jet was evaluated at different operating points invoked by varying the mass flow rate.

2.1 Numerical Method

The numerical investigations were carried out using OpenFoam®. The computational mesh was generated with approximately one million cells using the OpenFoam® implemented utility snappyHexMesh. Figure 1 shows the scaled computational domain and illustrates the boundary patches. The distance between the actuator outlet plane and the outlet patch of the domain was set to 1500 x l_{ref}, where the reference length describes the length of the actuator outlet slot ($l_{ref} = 0.013$ m). The key geometric parameters of the actuator are shown in figure 2 and summarized in table 1.

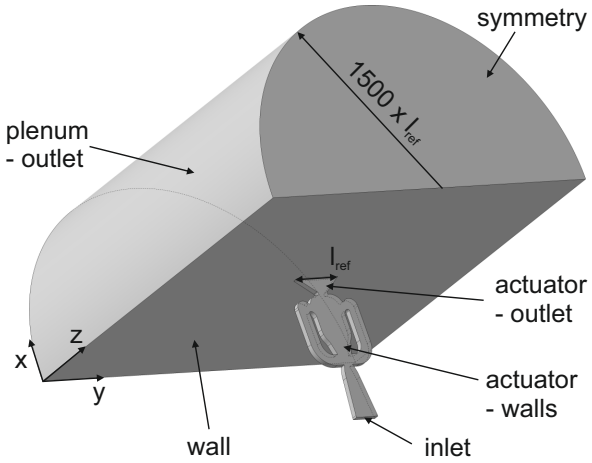

Fig. 1: Boundary conditions of the numerical domain.

The SWJ actuator is a self-oscillating device. Compressed air accelerates over the inlet nozzle and enters into the interaction zone. Caused by the Coandă effect [10], the fluid jet attaches to one side of the attachment walls and follows the curved surface to the exit nozzle, where the exit jet is formed. A fraction of the fluid enters the feedback channel and is led back to the interaction zone, where it pushes the attached jet to the opposite attachment wall. This process is repeated resulting in an oscillating jet. The characteristics of the oscillating jet depends on the internal geometry of the actuator and on the supply pressure ratio. SWJ actuator characteristics have already been investigated in various papers [11], [12], [13].
At high pressure ratios the compressed air gets pushed through the choked exit throat and forms an underexpanded jet. It was shown, that a super sonic sweeping jet is characterized by a limitation in its motion, which results in a reduced deflection angle θ of the actuators exit jet - compared to a sub sonic sweeping jet [12].
Tab. 2 lists the boundary conditions of the CFD simulation for the actuator at the design point. At the inlet a constant mass flow rate of $\dot{m} = 0.0025$ kg/s was set and the inlet temperature has a fixed value of $T = 293$ K. At the outlet patch a constant ambient pressure of $p = 101325$ Pa was predefined. With reference to [14] the Spalart-Allmaras turbulence model was chosen for modeling turbulent effects. A turbulence intensity of 1% is assumed and leads to a turbulent viscosity at the inlet patch of $\nu_t = 0.0011$ m^2/s. The boundary layer was modeled using the nutUSpaldingWallFunction on two boundary layer cells. The first cell of the mesh controls the $y+$ value. The dimension of the boundary layer cell was chosen to be $h_{bl} = 4.5$e-05 m. Therefore, the value of $y+$ resulted in a range of $y+ = 40 - 60$ where the wall function is applicable. Because of the high Mach numbers within the actuator, the sonicFoam solver was used to solve the compressible unsteady Reynolds-Averaged Navier-Stokes (URANS) equations. The adjustable time step of the CFD simulation was controlled by means of the threshold of a maximum courant number of $cou = 1$. For the CFD validation the position at $y = 0.2 \cdot l_{ref}$ at the outlet plane of the actuator was chosen - marked in figure 2.

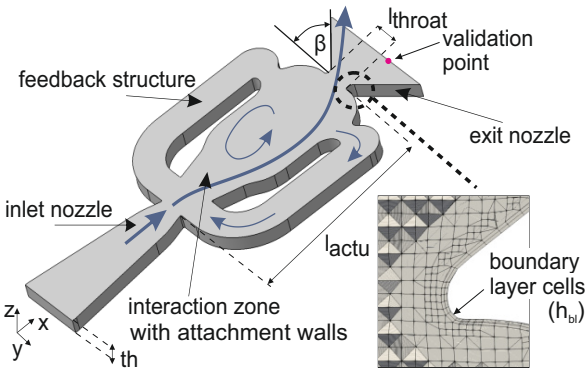

Fig. 2: Geometry of the sweeping jet actuator.

parameter	value	parameter	value
th	0.00139 m	l_{actu}	0.0193 m
l_{throat}	0.00278 m	l_{ref}	0.013 m
β	38°	h_{bl}	$4.5e-05$ m

Tab. 1: Geometrical parameters of the sweeping jet actuator.

	inlet	outlet	walls
U	$\dot{m} = 0.0025$ kg/s	zeroGradient	0 m/s
p	zeroGradient	101325 Pa	zeroGradient
T	293 K	zeroGradient	zeroGradient
ν_t	0.0011 m^2/s	zeroGradient	0 m^2/s

Tab. 2: Initial and boundary conditions of the CFD simulation at design point.

2.2 Experimental Validation Method

In order to build the sweeping jet actuator in original scale a stereolithographie 3D printing technique was used. For the experimental validation of the numerical simulation, a subminiature pitot probe with a dynamic kulite differential pressure transducer (XT-140M-1.7BARD) was used to measure the total pressure along the actuator outlet plane. Due to the small scale of the investigated SWJ actuator, it is challenging to capture the generated time-dependent velocity field in the required spatial resolution. For this reason, the pitot probe was only traversed along the actuator slot in span-wise direction (y-direction). The pitot probe was designed to have a frequency response of a Helmholtz resonator in an order of magnitude above the expected frequencies to be measured. For the validation, the mass flow rate through the actuator was set to $\dot{m} = 0.0025$ kg/s. It was measured by a FESTO SFAB-200 flow meter. The pressure ratio with regard to the inlet nozzle was PR = 3.6. To determine the local Mach number, the isentropic equation (equation 1) was used on the pressure measurements.

$$Ma = \sqrt{\left[\frac{p_0}{p_\infty}^{\frac{\kappa-1}{\kappa}} - 1\right] \cdot \frac{2}{\kappa - 1}}. \quad (1)$$

In super sonic flows with $Ma < 1.8$ the total pressure loss due to the occurring bow shock in front of the pitot probe is negligible [15]. Therefore, the Rayleigh pitot probe formula was not applied for this experiment. Figure 3 shows the time series of the pressure signal and the corresponding Mach number at the validation point (depicted in figure 2) - for both, the experimental measurement and the data computed by CFD simulation. Regarding the time series, which represent four oscillating periods of the actuator outlet jet, it is seen that the rising edges match well between both signals. Thus, it can be concluded that the oscillating frequency calculated by CFD simulation corresponds to the frequency acquired by the experimental measurements. Furthermore, it can be stated that the amplitudes of the simulated and measured signals are in good correspondence. The peak Mach number captured with the pitot probe at the validation point equals $Ma \approx 1.3$ while the minimum measured Mach number was $Ma \approx 0.5$.

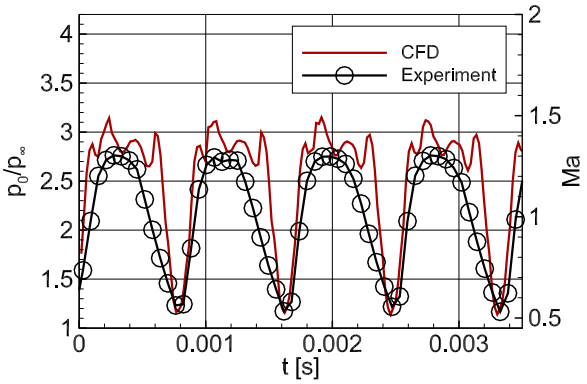

Fig. 3: SWJ actuator outlet signal – comparison of experimental and CFD results at $\dot{m} = 0.0025$ kg/s.

In order to analyze the frequency spectrum of the device, the time domain of the experimental measurement is converted to the frequency domain by means of a fast Fourier transform. The result is shown in figure 4, where the maximum of the amplitudes account for an actuator switching frequency of $f_{s,exp} = 1252$ Hz. The switching frequency which was extracted from the pressure signal computed by CFD simulation is $f_{s,cfd} = 1182$ Hz. The frequency deviation between both results yields Δf_s = 5.6%.

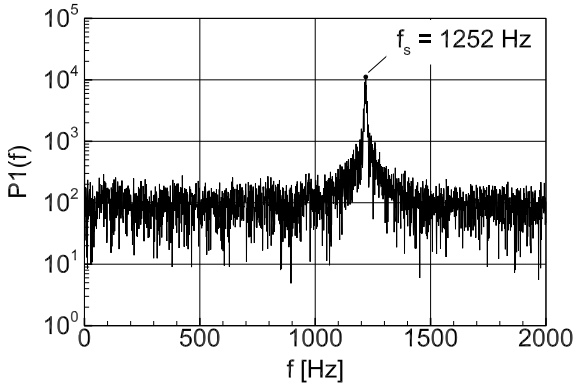

Fig. 4: Fast Fourier transform of actuator outlet signal - calculated from experimental measurement.

The dependency of the switching frequency and the supply mass flow rate of the fluidic device was examined by means of experimental pressure measurements, while the supply mass flow rate of the actuator was varied between $\dot{m} = 0.0011 - 0.0028$ kg/s. The resulting actuator characteristic is presented in figure 5. The trend shows a slightly increasing switching frequency and a rising peak Mach number at the actuator outlet with increasing mass flow rate.

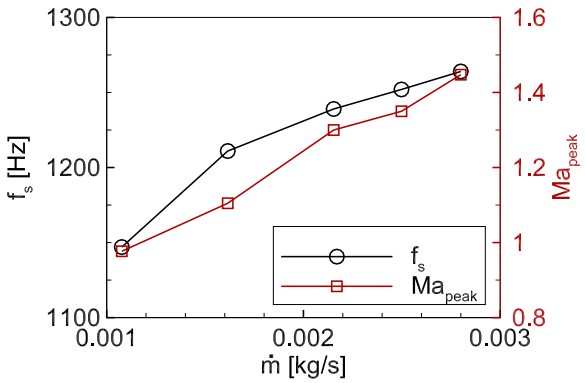

Fig. 5: Characteristics of sweeping jet actuator - calculated from experimental measurements.

Additionally, the numerical results have been validated using visualizations of the density gradients in y-direction within the actuator. The presented snapshots in figure 6 show the same phase angle of the actuator oscillation cycle, where the exit jet is centered inside the outlet nozzle. The supply pressure ratio was set to $PR = 3.6$. The experimentally acquired schlieren image depicted in figure 6a highlights coherent structures in the shear layer that are formed within the actuator [9]. Due to the high pressure ratio, the flow is choked at the exit throat and the compressed air generates an underexpanded jet within the outlet nozzle. The same flow structures are captured by the density gradients calculated from the numerical simulation – presented in figure 6b. However, due to the assumptions of the URANS simulation, the temporal and spatial resolution of the turbulent structures in the flow are suppressed to some extent.

Previous investigations [11] and [16] showed that a sub sonic jet is able to fully attach to the outlet nozzle walls and that the sweeping motion of the actuator jet is reduced by an increasing supply pressure ratio. The flexibility of the actuator jet is expressed by the jet deflection angle θ that is defined in [16] as the angle between the actuator center line and the center line of the exit jet. Figure 7 presents the computed Mach number distribution within the SWJ actuator. In figure 7a, a snapshot capturing the instantaneous moment of the maximum jet deflection is shown. A maximum Mach number of $Ma = 1.6$ is reached downstream of the exit throat within the outlet nozzle. This leads to a limitation in motion of the actuator sweeping jet. Thus, the jet is not capable of attaching to the nozzle diffusor walls. As derived from the time-averaged flow field in figure 7b, the maximum deflection angle of the computed actuator jet was $\theta \approx 13°$.

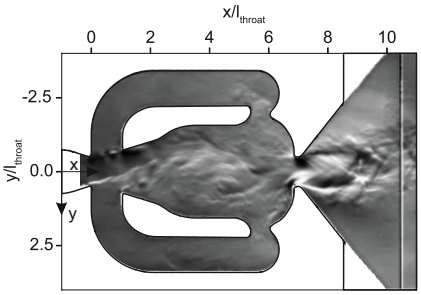

(a) Schlieren visualization acquired from experimental measurement; image extracted from [9].

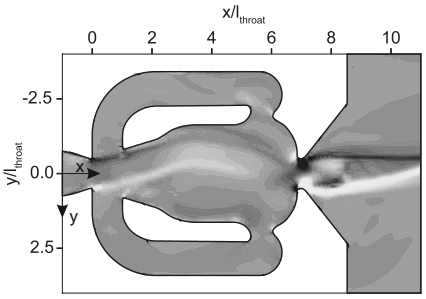

(b) Density gradient from CFD simulation.

Fig. 6: Comparison of computed density gradients and schlieren visualizations at $PR = 3.6$.

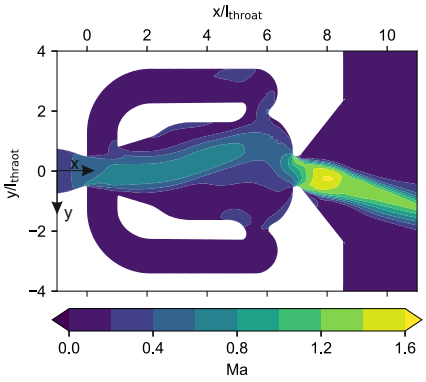

(a) Instantaneous - moment of maximum jet deflection.

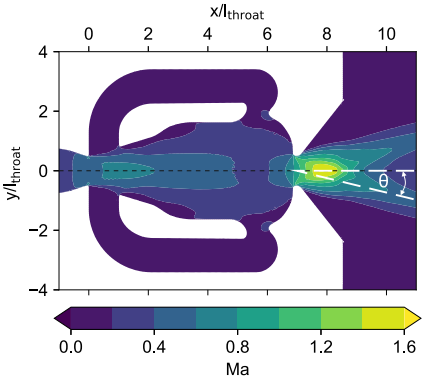

(b) Time averaged flow field.

Fig. 7: Mach number distribution at $PR = 3.6$.

3 HALF-DIFFUSOR RAMP - WIND TUNNEL EXPERIMENTS

In the current approach, the effect of active flow control by a configuration of two self switching SWJ actuators - which have not been synchronized - was investigated. The test section of the wind tunnel experiments features a half-diffusor ramp producing a turbulent pressure-induced separated flow in a transonic Mach number regime.

3.1 Experimental Setup

The experimental investigations were carried out at the transonic wind tunnel at the chair of Aerodynamics. This indraft wind tunnel is suitable for investigations in a transonic and super sonic flow regime with inflow Mach numbers up to $Ma = 2.4$. Various nozzles and measuring sections are available for this purpose. The wind tunnel test section used for this experiment has a cross section of 0.15 m x 0.15 m. The geometrical details of the ramp used in the experiment are depicted in figure 8.

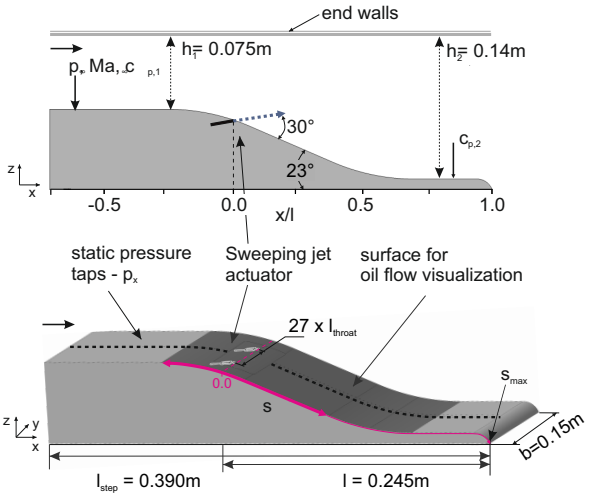

Fig. 8: Geometrical details of the ramp producing an adverse pressure gradient.

The ramp inclination angle was $23°$, which led to a pressure-induced flow separation downstream of the onset of the ramp. Moreover, the boundary layer is turbulent because of a trip at the inlet of the test section. For the application of active flow control, two SWJ actuators are installed symmetrically with respect to the center line of the ramp. The distance between the outlet orifices was 27 x l_{throat}. Seifert and Pack [17] showed that the optimal position of the actuator slot is shortly upstream or directly at the time averaged separation line. Therefore, the actuator outlets are located at the onset of separation at the position $x/l = 0$. The blowing angle was set to $30°$ in reference to the surface of the ramp.
One important parameter influencing the pressure rise over the ramp is the expansion ratio (ER). Defined by means of the relation between h_2 to h_1, the expansion ratio is $ER = 1.87$. Brederode and Bradshaw [18] define the aspect ratio (AR) as the width-height ratio of the ramp and they state that this should not fall below a value of 10 in order to still assume a 2D flow. With the given values of $b = 0.15$ m for the width and $h_1 = 0.075$ m for the inlet height of the ramp, the aspect ratio results to $AR = 2$. Thus, with an AR of less than 10, the experiments are based on complex secondary flow structures (3D flows) influencing the reattachment length of the separated flow. The diffusor section of the ramp features 68 static pressure taps implemented along the center line of the ramp which are shown in figure 8. All pressures are measured as absolute pressure values.
The inflow Mach number was calculated from the total pressure measured in the settling chamber and the static pressure tap located at $x/l = -0.65$. Within the scope of the experimental work presented in this paper, inflow Mach numbers ranging from $Ma = 0.3$ to $Ma = 0.8$ were investigated. The corresponding Reynolds numbers of $Re = 0.4 - 1.1 \cdot 10^6$ are based on the step height of the ramp ($\Delta h = h_2 - h_1$).
One prominent parameter to compare various configurations of an active flow control system is the non-dimensional momentum coefficient c_μ, as defined by Bauer for incompressible flows [19]. It relates the momentum of the actuators to a reference momentum. For the utilization in a compressible flow regime, the momentum coefficient was modified. Therefore, the compressible momentum coefficient c_μ is calculated using equation 2.

$$c_\mu = \frac{\dot{m}_{afc} \cdot Ma_{jet} \cdot \sqrt{\kappa \cdot R \cdot T_{jet}}}{\dot{m}_{ref} \cdot Ma_\infty \cdot \sqrt{\kappa \cdot R \cdot T_\infty}} \tag{2}$$

Figure 9 shows the dependency of the momentum coefficient from the inflow Mach number and the mass flow rate of the actuation system. The momentum coefficient decreases with increasing inflow Mach number and increases with the mass flow rate of the actuation system. The marked dots indicate the operating points of the actuator system as it was configured in the experiments for the results presented hereinafter.

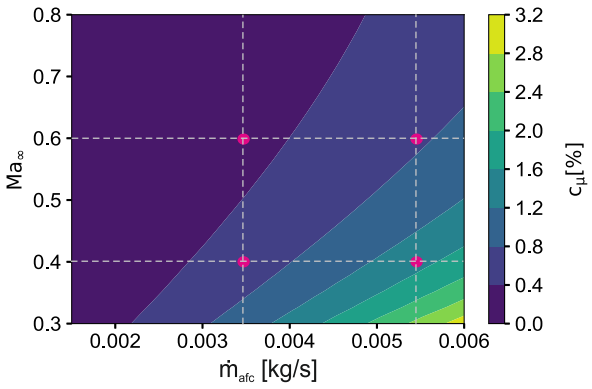

Fig. 9: Distribution of the momentum coefficient depending on the inflow Mach number and the actuator mass flow rate.

3.2 Oil Flow Visualization

The results of the oil flow visualization for the inflow Mach numbers $Ma = 0.4$ and $Ma = 0.6$ are presented in figure 10 and 11. For each inflow Mach number the condition with no actuation (reference flow) and with active flow control are compared. The mass flow rate of the actuation system, with two SWJ actuators working in parallel, was set to $\dot{m}_{afc} = 0.0055$ kg/s. This results in a momentum coefficient of $c_\mu = 1.5\%$ for $Ma_\infty = 0.4$ and of $c_\mu = 0.78\%$ for $Ma_\infty = 0.6$. The wall streamlines that were derived from the oil flow visualization indicate the direction of the time averaged wall shear stress and illustrate the global flow structures over the ramp. Figure 10 a) and figure 11 a) show that the flow separation starts at the actuator slots at $s/s_{max} = 0$ and propagates along the ramp in case of no actuation.
It is also seen that the flow pattern over the ramp is formed asymmetrically to the center line of the ramp. Furthermore, the flow pattern is characterized by a large area of separated flow, which is dominated by secondary flow structures. The flow separation is decisively created by a massive passage vortex rotating in counter clock-wise direction, which is blocking the passage over the ramp. According to vortex theory, a second – much smaller – vortex rotating in clock-wise direction is formed upstream of the passage vortex. The development of the pair of vortices significantly influences the flow pattern on the ramp. Also, it is apparent that the flow pattern feature very similar structures for both investigated Mach numbers.

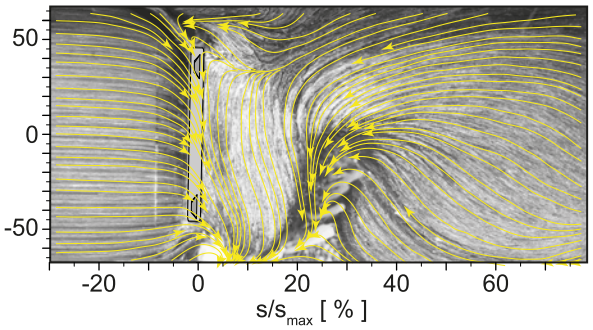

(a) Reference flow - no active flow control.

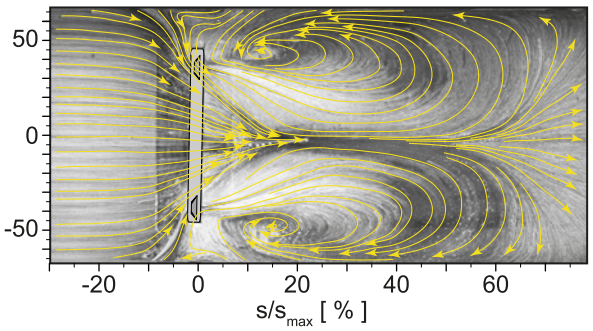

(b) Active flow control with $\dot{m}_{afc} = 0.0055$ kg/s.

Fig. 10: Oil Flow Visualization at $Ma_\infty = 0.4$ – for the reference flow and with AFC.

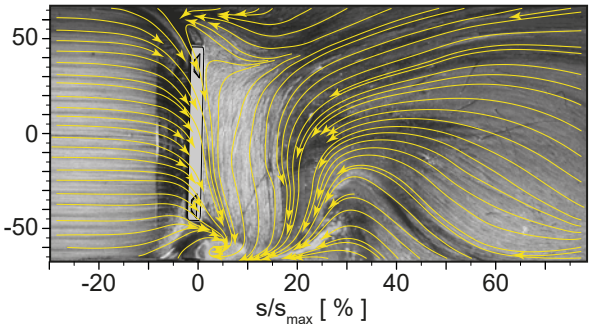

(a) Reference flow - no active flow control.

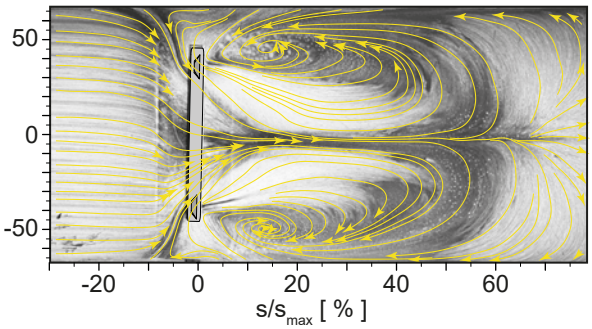

(b) Active flow control on - $\dot{m}_{afc} = 0.0055$ kg/s.

Fig. 11: Oil Flow Visualization at $Ma_\infty = 0.6$ – for the reference flow and with AFC.

Figures 10 b) and 11 b) present the corresponding state with active flow control. The presence of oil color paint in different shadings provides further insight to the time averaged wall shear stress distribution. In the mid section of the test specimen the streamlines are more guided in the main flow direction indicating the flow to be reattached. The flow separation was suppressed successfully and the passage blocking was reduced by means of the actuation. In addition, two large corner vortices (secondary flows) are formed on the upper and lower end wall. These protrude into the mid section to some extent, affecting the flow field by restricting the channel flow. Considering the center line of the test section, the flow patterns are formed symmetrically by the actuation. The two corner vortices are growing similar in size.
Quantitative studies to the effect and the efficiency of the active flow control system are conducted by means of static pressure measurements and are presented hereinafter.

3.3 Pressure Measurements

The pressure coefficient for compressible flows along the center line of the ramp is calculated using equation 3,

$$c_p = \frac{2}{\kappa Ma_\infty^2}\left(\frac{p_x}{p_\infty} - 1\right). \tag{3}$$

Figure 12 shows the static pressure distribution for the reference flow and figure 13 for the actuated flow at three different inflow Mach numbers. Here, the measured data of the pressure taps and the corresponding curve fitting are plotted. In all cases, the flow accelerates until the suction

peak is formed at $x/l = -0.2$. It is assumed that the acceleration of the flow is induced by the growing boundary layer along the inlet oft the ramp. Downstream of the suction peak, the flow decelerates due to the diffusor effect, which results in a significant increase of static pressure. Due to the actuator insert – between $-0.17 < x/l < 0.085$ – no pressure information were available.

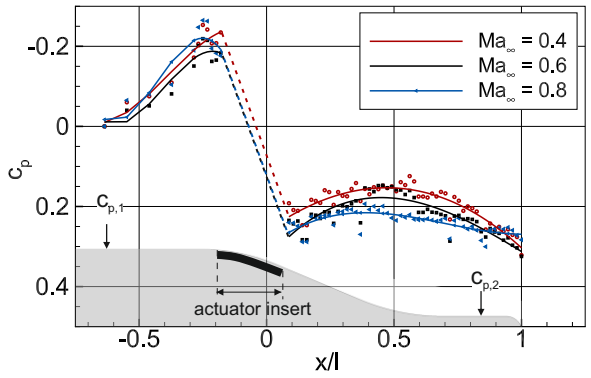

Fig. 12: Static pressure coefficient of the reference flow with no active flow control - at different inflow Mach numbers.

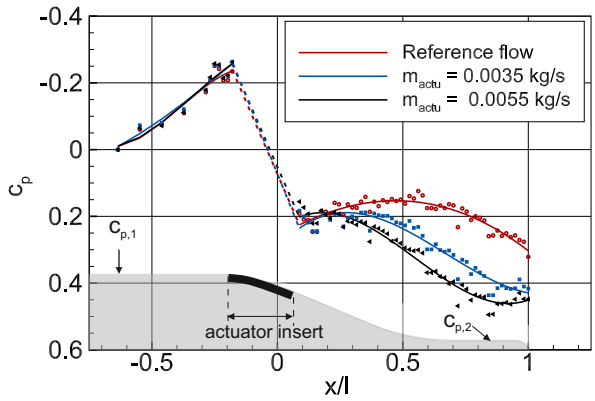

(a) $Ma_\infty = 0.4$.

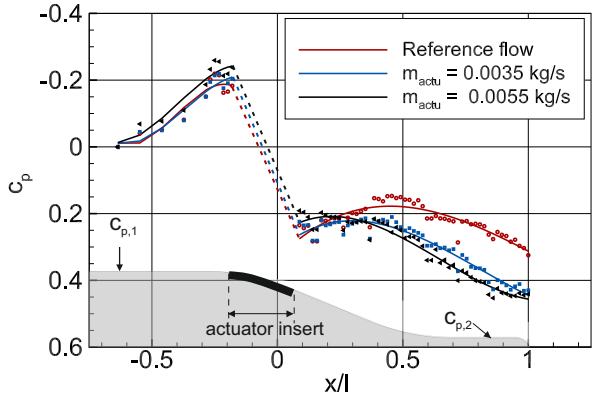

(b) $Ma_\infty = 0.6$.

Fig. 13: Static pressure coefficient for the reference flow and with AFC - at two different inflow Mach numbers.

For the reference flow, the static pressure slightly decreases from $x/l = 0.085$ until $x/l = 0.45$ downstream of the actuator insert. It can be assumed, that the blocking effect of the flow separation affects the pressure recovery. Furthermore, the pressure recovery over the ramp was only slightly dependent of the inflow Mach number.
The effect of active flow control on the pressure coefficient along the ramp is shown in figure 13. Here, two different mass flow rates were used and the inflow Mach number of $Ma_\infty = 0.4$ (a) and $Ma_\infty = 0.6$ (b) has been set. It can be seen that the momentum of the actuator jet has a positive impact on the pressure rise along the center line of the ramp. Downstream of the actuator slots a slight pressure drop at $x/l = 0.085$ occurs. Subsequently, a distinct static pressure rise from $x/l = 0.2$ to $x/l = 1$ was observed. Compared to the reference flow, it can be seen that the higher the mass flow rate of the actuation system gets, the higher the pressure rise over the ramp was.

The contour plots in figure 14 present the change of the pressure coefficient Δc_p along the ramp with AFC. The impact of a variation of the momentum coefficients of the AFC to the static pressure is calculated by means of equation 4. Here, the pressure coefficient of the reference flow is subtracted from the one with actuation. Positive values of Δc_p represent a pressure gain and values of $\Delta c_p < 0$ depict a reduction in static pressure with respect to to the reference flow.

$$\Delta c_p(c_\mu, x/l) = c_{p,acf}(c_\mu, x/l) - c_{p,ref}(x/l) \tag{4}$$

Figure 14a shows the contour plot of the changing static pressure gains for an inflow Mach number of $Ma_\infty = 0.4$. Here, the values of the momentum coefficient ranges from $0.08\% < c_\mu < 1.5\%$. The position of the actuator slots are marked by the dashed line. The red line defines the minimum momentum coefficient which is required to generate a significant pressure gain of $\Delta c_p > 0.2$ at some point along the ramp. It can be seen, that an effort of $c_\mu \geq 0.9\%$ causes a high pressure gain of $\Delta c_p \geq 0.2$ at the end of the ramp. Furthermore, the actuator jet causes a decreased suction peak upstream of the actuator slots with momentum coefficients of $c_\mu \geq 0.9\%$. For values of $c_\mu < 0.9\%$ the actuation increases the suction peak ($\Delta c_p < 0$) upstream of the actuator slots. The maximum static pressure gain of $\Delta c_p = 0.26$ was reached at the end of the ramp by a momentum coefficient of $c_\mu = 1.5\%$.
The contour plot of the change of the pressure coefficient for an inlet Mach number of $Ma = 0.6_\infty$ is shown in figure 14b. Due to the higher inlet Mach number, the values of the momentum coefficient were varied between $0.04\% < c_\mu < 0.79\%$. Nevertheless, the trend of the pressure coefficient is very similar when compared to the lower Mach number – figure 14a. Downstream of the ramp the pressure gain increases due to the higher momentum coefficients. Here, the maximum pressure gain is $\Delta c_p = 0.17$ at a momentum coefficient of $c_\mu = 0.79\%$. Besides, it can be seen that an increased suction peak occurs upstream of the actuator slots over the entire actuator operating points ($\Delta c_p < 0$).

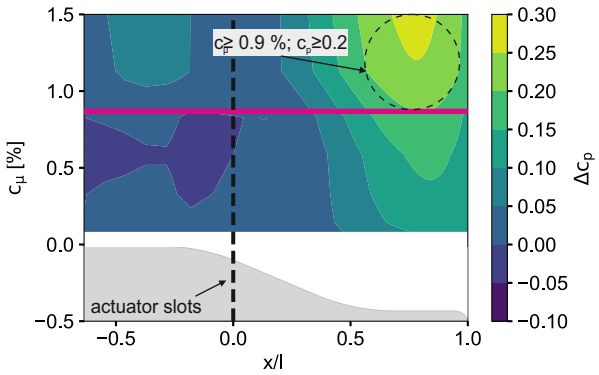

(a) $Ma_\infty = 0.4$.

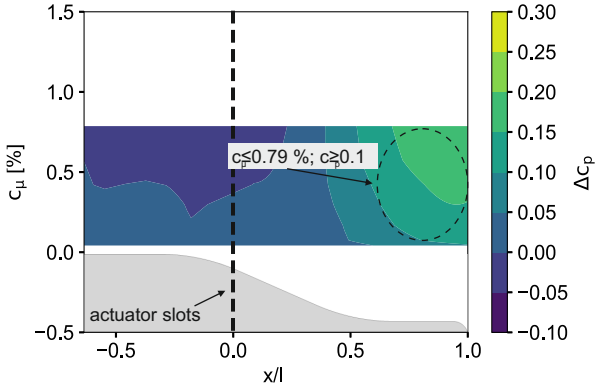

(b) $Ma_\infty = 0.6$.

Fig. 14: Static pressure gain distribution along the center line of the ramp at different momentum coefficients.

The parameter η indicates the ratio between the static pressure rise over the ramp and a theoretical value $c_{p,c}$ – equation 5. In the following, the parameter η will be referred to as ramp coefficient. Based on an incompressible flow, the theoretical value represents the maximum static pressure rise over a $90°$ diffusor – equation 6 according to [20]. The static pressure rise over the ramp is related to a point upstream of the ramp $c_{p,1}$ at $x/l = -0.65$ and a point downstream of the ramp $c_{p,2}$ at $x/l = 0.85$ – labeled in figure 12 and 13.

$$\eta = \frac{(c_{p,2} - c_{p,1})}{c_{p,c}} \tag{5}$$

$$c_{p,c} = \frac{2}{ER} \cdot (1 - \frac{1}{ER}), \quad ER = 1.87 \tag{6}$$

Figure 15 presents the ramp coefficient in relation to the inlet Mach number – with and without AFC. In case of AFC, the mass flow rate of the AFC system is set constant to $\dot{m}_{afc} = 0.0055$ kg/s. In addition, the trend of the velocity ratio is shown – equation 7.

$$VR = \frac{Ma_{jet,peak}}{Ma_\infty} \tag{7}$$

For the reference flow (η - afc off), the ramp coefficient equals $\eta = 0.47$ at $Ma_\infty = 0.3$. That signifies that the static pressure rise over the ramp is reduced to 47% of the theoretical pressure rise of a Carnot diffusor ($\eta = 1$) - due to secondary flow structures. The ramp coefficient increases slightly for higher inlet Mach numbers up to a maximum of $\eta = 0.55$ at $Ma = 0.8$.
Switching on the actuation system led to a ramp coefficient of up to $\eta = 0.99$ at $Ma = 0.3_\infty$. Here the effectiveness improvement amounts to $\Delta\eta = 0.52$. Applying AFC, led to the theoretical pressure recovery of a Carnot diffusor. However, at higher inlet Mach numbers the ramp coefficient is decreasing. Here, an improvement of $\Delta\eta = 0.29$ at $Ma = 0.8$ was measured when using AFC. At a constant mass flow rate of the actuation system the actuator jet Mach number is maintained constant and consequently the velocity ratio is decreasing with higher inlet Mach numbers.

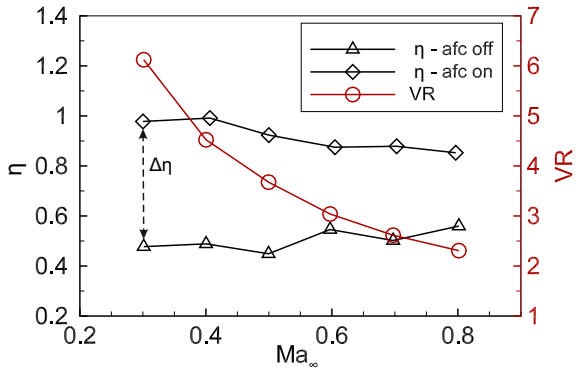

Fig. 15: Ramp coefficient and velocity ratio at different inlet Mach numbers with $\dot{m}_{afc} = 0.0055$ kg/s.

The ramp coefficient indicated the effectiveness of the AFC system and does not consider the momentum flux injected into the flow by the AFC system.
Taking the effort of the actuation system into account, a Figure of Merit (FM) is introduced (equation 8) [21]. Here, the energy conversion of the system with active flow control ΔP_{afc} is related to the sum of the energy conversion of the system without active flow control $\Delta P_{no,afc}$ and the added energy of the actuator jet power ΔP_{jet}. The energy of the system with and without active flow control is expressed by equation 9, where the pressure coefficient $c_{p,2}$ is measured downstream of the ramp. The inlet velocity u_1 and the actuator jet peak velocity $u_{jet,peak}$ was calculated based on the isentropic flow equation with the corresponding Mach number. The actuator jet power ΔP_{jet} is defined by equation 10.

$$FM = \frac{\Delta P_{afc}}{\Delta P_{no,afc} + \Delta P_{jet}} \tag{8}$$

$$\Delta P = c_{p,2} \cdot \dot{m} \cdot \frac{u_1^2}{2} \tag{9}$$

(10) $$\Delta P_{jet} = \dot{m}_{jet} \cdot \frac{u_{jet,peak}^2}{2}$$

The resulting FM with respect to the momentum coefficient is shown in figure 16 for both investigated inflow Mach numbers. In both cases, the FM is rising intensely up to momentum coefficients of $c_\mu = 0.15\%$. Adding more momentum into the flow by the AFC system shows minor effects on the FM. The maximum value of the FM indicates the most effective actuation set up within the investigated regime. A maximum of $FM = 1.78$ is reached at a momentum coefficient of $c_\mu = 1.1\%$ ($Ma_\infty = 0.4$) and a maximum of $FM = 1.54$ is attained at a momentum coefficient of $c_\mu = 0.6\%$ ($Ma_\infty = 0.6$).

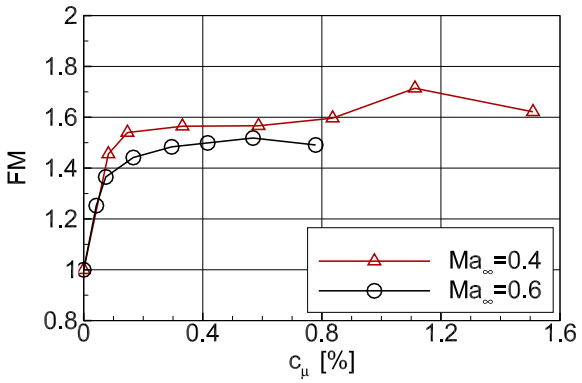

Fig. 16: Figure of Merit dependency on the momentum coefficient.

4 CONCLUSIONS

In the present paper, a CFD simulation of the inner flow field of a sweeping jet actuator was performed using OpenFoam®. The numerical calculations were verified by dynamic pressure measurements at the actuator outlet slot. The characteristics of the actuator outlet signal showed a high level of agreement between the experiments and the CFD simulation. The switching frequency of the SWJ actuator was $f_s \approx 1200$ Hz at a pressure ratio of $PR = 3.6$. The computed density gradients of the actuators inner flow field corresponded well with the schlieren visualizations from Hirsch et al. [9]. It was shown that the flow was choked at the actuator exit throat. Due to the compressed air within in the actuator an underexpanded exit jet was formed downstream of the throat, featuring a maximum deflection angle of approximately $\theta = 13°$. The distribution of the Mach number indicated a peak Mach number at the actuators outlet plane of $Ma \approx 1.3$.

Two SWJ actuators were implemented in a half-diffusor ramp featuring a blowing angle with respect to the surface of $30°$. Oil flow visualization showed that the flow separated at the actuator slots – in case of no actuation. Downstream, an asymmetrically flow pattern was formed. The pattern demonstrated that the flow is reattaching and the flow separation was suppressed successfully in the mid section of the ramp by means of AFC.

A quantitative prediction of the effect of AFC is presented by the results of the static pressure measurements. It was shown that the actuation has a positive effect regarding the pressure rise over the ramp. At an inflow Mach number of $Ma_\infty = 0.4$, the actuation system ensured a decisive pressure rise of $\Delta c_p > 0.2$ downstream of the ramp at an effort of $c_\mu \geq 0.9\%$. The maximum pressure gain for $Ma_\infty = 0.6$ was $\Delta c_p = 0.17$ with a maximum momentum coefficient of $c_\mu = 0.78\%$. Taking the ramp coefficient into account, it can be manifested that an improvement of $\Delta\eta = 0.52$ at $Ma = 0.3$ and an improvement of $\Delta\eta = 0.29$ at $Ma = 0.8$ was realized. Furthermore, it was shown that the theoretical pressure coefficient produced by a Carnot-diffusor was reached by means of active flow control ($\eta = 0.99$). In order to consider the efficiency of the AFC system – the Figure of Merit was calculated. The results indicated a large performance increase for small momentum coefficients up to $c_\mu = 0.15\%$ at both investigated Mach numbers $Ma = 0.4$ and $Ma = 0.6$. A further increase of the momentum only induces a slight rise of the Figure of Merit. At $Ma_\infty = 0.4$ a maximum of $FM = 1.78$ is approached by a momentum coefficient of $c_\mu = 1.1\%$. For the higher inflow Mach number of $Ma_\infty = 0.6$ a maximum of $FM = 1.54$ is attained by a momentum coefficient of $c_\mu = 0.6\%$.

The beneficial effect of active flow control by means of a super sonic actuator exit jet on a separated flow was shown successfully in a compressible Mach number regime. The pressure-induced separated flow has been forced to reattach in the mid section of the ramp and a pressure gain along the ramp was produced due to AFC.

NOMENCLATURE

b	width [m]
c_μ	momentum coefficient [%]
c_p	pressure coefficient [-]
$c_{p,c}$	carnot pressure coefficient [-]
cou	courant number [-]
f	frequency [Hz]
Δf	frequency deviation [Hz]
h	height [m]
h_{bl}	boundary layer height [m]
l	length [m]
$\dot{m}$	mass flow rate [kg/s]
Ma	Mach number [-]
p	pressure [Pa]
ΔP	energy conversion [kg · m^2 / s^3]
R	specific gas constant for air [J/(kg K)]
Re	Reynoldsnumber [-]
s	length from actuator slot [m]
T	temperature [K]
t	time [s]
th	thickness [m]
u	velocity [m/s]
x, y, z	coordinates [m]

Symbols

β	angle actuator outlet nozzle [°]
η	efficiency of ramp [-]

θ	deflection angle [°]
κ	ratio of specific heat [-]
ν_t	turbulent viscosity [m^2/s]

Indices

$actu$	actuator
afc	active flow control
jet	actuator exit jet
max	maximum
ref	reference
s	switching
$throat$	smallest cross section
∞	ambient
1	inlet
2	outlet

Abbreviations

AFC	active flow control
AR	aspect ratio
CCW	counter clock wise
CFD	computational fluid dynamics
ER	expansion ratio
EXP	experiment
FM	Figure of Merit
HPC	high pressure compressor
ILR	Institute for Aeronautics and Astronautics
LPC	low pressure compressor
PR	pressure ratio
TRL	technology readiness level
VR	velocity ratio

Acknowledgement

The authors gratefully acknowledge support by the Deutsche Forschungsgemeinschaft (DFG) as part of collaborative research centre CRC 1029 "Substantial efficiency increase in gas turbines through direct use of coupled unsteady combustion and flow dynamics".

REFERENCES

[1] T. R. Troutt, S. Bhattacherjee and B. Scheelke, 'Modification of vortex interactions in a reattaching separated flow', *AIAA Journal*, vol. 24, no. 4, pp. 623–629, 1986, ISSN: 0001-1452. DOI: 10.2514/3.9317.

[2] H. Nagib, J. Kiedaisch, P. Reinhard and B. Demanett, 'Control Techniques for Flows with Large Separated Regions: A New Look at Scaling Parameters', in *3rd AIAA Flow Control Conference*, [Reston, VA]: [American Institute of Aeronautics and Astronautics], 2006, p. 9, ISBN: 978-1-62410-036-9. DOI: 10.2514/6.2006-2857.

[3] C. Hah and J. Loellbach, 'Development of Hub Corner Stall and Its Influence on the Performance of Axial Compressor Blade Rows', *Journal of Turbomachinery*, vol. 121, no. 1, p. 67, 1999, ISSN: 0889-504X. DOI: 10.1115/1.2841235.

[4] V. Zander and W. Nitsche, 'Control of secondary flow structures on a highly loaded compressor cascade', *Proceedings of the Institution of Mechanical Engineers, Part A: Journal of Power and Energy*, vol. 227, no. 6, pp. 674–682, 2013. DOI: 10.1177/0957650913495538.

[5] P. Schloesser, V. Soudakov, M. Bauer and J. Wild, 'Active Separation Control at the Pylon-Wing Junction of a Real-Scale Model', *AIAA Journal*, vol. 57, no. 1, pp. 132–141, 2019, ISSN: 0001-1452. DOI: 10.2514/1.J057345.

[6] S. Löffler, M. Staats, T. Grund and J. Weiss, 'Increasing the Effectiveness of a Vertical Stabilizer by Combining Pulsed Jet Actuation at the Leading Edge and the Rudder Hinge Line', in *2018 Applied Aerodynamics Conference*, Reston, Virginia: American Institute of Aeronautics and Astronautics, 6252018, ISBN: 978-1-62410-559-3. DOI: 10.2514/6.2018-2854.

[7] E. A. Whalen, M. Spoor, P. M. Vijgen, J. Tran, A. Shmilovich, J. C. Lin and M. Andino, 'Full-scale Flight Demonstration of an Active Flow Control Enhanced Vertical Tail', in *8th AIAA Flow Control Conference*, Reston, Virginia: American Institute of Aeronautics and Astronautics, 6132016, ISBN: 978-1-62410-432-9. DOI: 10.2514/6.2016-3927.

[8] Z. Trávníček, V. Cyrus, D. Šimurda, M. Luxa, J. Lukáč and J. Kordík, 'Experimental Investigation of the Compressor Cascade under an Active Flow Control', *EPJ Web of Conferences*, vol. 45, p. 01 086, 2013. DOI: 10.1051/epjconf/20134501086.

[9] D. Hirsch, E. C. Graff and M. Gharib, *Compressible Flows in Fluidic Oscillators*, 2013. [Online]. Available: arxiv.org/abs/1310.3310 (visited on 04/08/2019).

[10] H. M. Coandă, 'Device for deflecting a stream of elastic fluid projected into an elastic fluid: A', US 2.052.869 A, 1936. (visited on 23/08/2019).

[11] D. Hirsch and M. Gharib, 'Schlieren Visualization and Analysis of Sweeping Jet Actuator Dynamics', *AIAA Journal*, vol. 56, no. 8, pp. 2947–2960, 2018, ISSN: 0001-1452. DOI: 10.2514/1.J056776.

[12] M. Koklu, 'The Effects of Sweeping Jet Actuator Parameters on Flow Separation Control', in *45th AIAA Fluid Dynamics Conference*, Reston, Virginia: American Institute of Aeronautics and Astronautics, 6222015, ISBN: 978-1-62410-362-9. DOI: 10.2514/6.2015-2485.

[13] R. Woszidlo and I. J. Wygnanski, 'Parameters Governing Separation Control with Sweeping Jet Actuators', in *29th AIAA Applied Aerodynamics Conference*, [Reston, VA]: [American Institute of Aeronautics and Astronautics], 2011, p. 287, ISBN: 978-1-62410-145-8. DOI: 10.2514/6.2011-3172.

[14] M. Staats, S. Löffler, C. Ebert, T. Grund and J. Weiss, 'A Fluidic Device for Active Flow Control: Simulation vs. Experiment with Emphasis on Application', in *2018 Applied Aerodynamics Conference*, Reston, Virginia: American Institute of Aeronautics and Astronautics, 6252018, p. 247, ISBN: 978-1-62410-559-3. DOI: 10.2514/6.2018-3336.

[15] D. A. Caughey, *Review of Compressible Flow Topics*, Ithaca, New York, United States. [Online]. Available: https://www.researchgate.net/publication/267418667_Review_of_Compressible_Flow_Topics (visited on 04/08/2019).

[16] S. Park, H. Ko, M. Kang and Y. Lee, 'An Experimental Study of the Characteristics of a Supersonic Fluidic Oscillator Utilizing the Design of Experiment', in *AIAA Aviation 2019 Forum*, Reston, Virginia: American Institute of Aeronautics and Astronautics, 6172019, p. 281, ISBN: 978-1-62410-589-0. DOI: 10.2514/6.2019-3395.

[17] A. Seifert and L. G. Pack, 'Compressibility and Excitation Location Effects on High Reynolds Numbers Active Separation Control', *Journal of Aircraft*, vol. 40, no. 1, pp. 110–119, 2003, ISSN: 0021-8669. DOI: 10.2514/2.3065.

[18] V. de Brederode and P. Bradshaw, *Three-dimensional flow in nominally two-dimensional separation bubbles part 1: Flow behind a rearward-facing step*, London and United Kingdom, 1972.

[19] M. Bauer, 'Design and Application of a Fluidic Actuator System for High-lift Flow Control', Doctoral Dissertation, Technische Universität Berlin, Berlin, Germany, 2015-06-05. [Online]. Available: https://depositonce.tu-berlin.de/bitstream/11303/4796/2/bauer_matthias.pdf (visited on 24/01/2017).

[20] F. Schmitt, 'Untersuchung der turbulenten Stufenströmung bei hohen Reynoldszahlen', Zugl.: Karlsruhe, Univ., Diss. : 1986, Düsseldorf, 1986.

[21] M. Staats and W. Nitsche, 'Experimental Investigations on the Efficiency of Active Flow Control in a Compressor Cascade With Periodic Non-Steady Outflow Conditions', in *Proceedings of the ASME Turbo Expo: Turbine Technical Conference and Exposition - 2017*, New York, N.Y.: The American Society of Mechanical Engineers, 2017, V02AT39A006, ISBN: 978-0-7918-5078-7. DOI: 10.1115/GT2017-63246.